Towards efficient elastic actuation in bio-inspired robotics using dielectric elastomer artificial muscles

To cite this article before publication: Chongjing Cao *et al* 2019 *Smart Mater. Struct.* in press https://doi.org/10.1088/1361-665X/ab326b

Towards efficient elastic actuation in bio-inspired robotics using dielectric elastomer artificial muscles

Chongjing Cao[1 2 *], Xing Gao[2 3 4] and Andrew T. Conn[2 3 *]

[1] Department of Aerospace Engineering, University of Bristol, UK

[2] Bristol Robotics Laboratory, Bristol, UK

[3] Department of Mechanical Engineering, University of Bristol, UK

[4] Shenzhen Institute of Advanced Technology, China Academic of Sciences, Shenzhen, China

* Emails: C. Cao (cc15716@bristol.ac.uk); A. Conn (a.conn@bristol.ac.uk)

Abstract

In nature, animals reduce their cost of transport by utilizing elastic energy recovery. Emerging soft robotic technologies such as dielectric elastomer actuators (DEAs) offer an advantage in achieving biomimetic energy efficient locomotion thanks to their high actuation strain and inherent elasticity. In this work, we conduct a comprehensive study on the feasibility of using antagonistic DEA artificial muscles for bio-inspired robotics. We adopt a double cone DEA configuration and develop a mathematical model to characterize its dynamic electromechanical response. It is demonstrated that this DEA design can be optimized in terms of the maximum work output by adjusting the strut height design parameter. Using this optimized design, we analyse the power/stroke output and the electromechanical efficiency of the DEA and show how these actuation characteristics can be maximized for different payload conditions, excitation frequencies and actuation waveforms. The elastic energy recovery from the DEA is then demonstrated by reducing the duty ratio of the actuation signal and thus allowing the stored elastic energy in the DEA membranes to contribute to the work output. A bio-inspired three-segment leg prototype driven by the same actuator is presented to demonstrate that the same energy recovery principle is feasible for bio-inspired robotics.

Key words: dielectric elastomer actuator, energetic study, elastic energy recovery, bio-inspired locomotion, soft robotics

1. Introduction

In nature, animals often exploit inherent compliance and elastic energy storage to minimize cost of transport and maximize stability. For example, legged animals take advantage of their serial muscle and tendon complex in their limbs, and in a running gait, kinetic and gravitational potential energy is stored as elastic energy in tendons in limbs when an animal hits the ground, and then released in the second half of the step to reduce the work requirement from the muscles [1]. Most species of flying insects utilize their inherently elastic thorax and excite their muscle-thorax oscillator at its resonant frequency to amplify the flapping stroke and greatly reduce inertial power demands [2].

Bioinspired robotics take these concepts from nature and apply them to robotic systems. Many bioinspired robots that utilize the feature of elasticity have emerged over the last 30 years. For example, legged robots with elastic elements connected to the actuation systems in series (e.g. BigDog [3], Puppy II [4], Cheetah-cub [5]) and flapping wing micro air vehicles mimicking the resonant actuations of insects (e.g. Harvard RoboBee [6]). Despite the advancement in bioinspired robotics, most robotic designs adopt rigid actuators while the compliance is included by adding additional springs to the robotic system.

Emergent soft robotic technologies such as dielectric elastomer actuators (DEAs) offer an alternative paradigm for bioinspired robotic designs. Firstly, DEAs achieve large actuation strains that are similar to muscles [7]. Secondly, the inherent elasticity of the material makes DEAs capable of storing and releasing elastic energy, just like tendons but without the need for a separate elastic serial element. In addition, compact multi-degree-of-freedom (DOF) actuators that mimic the antagonistic muscle groups can be achieved using DEAs. For example, the spring roll design with 2-DOF [8], a 5-DOF cone DEA [9] [10], and a 6-DOF elastic cube actuator [11]. Other advantages of DEAs over conventional actuators include high energy density, scalability and low cost [12].

In recent years, many DEA actuated bioinspired robots have been developed. For example, earthworm inspired peristaltic crawling robots [13] [14] and inchworm inspired two-anchor crawling robots [15] [16] [17]. Legged DEA-driven hexapod robots include FLEX1 and FLEX 2 [18], MERbot driven by multi-DOF rolled DEAs [19] and S-Hex I and II driven by multi-DOF double cone actuators [20] [21] [22]. Underwater actuation of DEAs was made possible by isolating high voltage electrodes from water and several DEA driven swimming robots were developed to mimic the undulation motion [23] [24] and jet propulsion [25]. The resonant actuation of DEAs has also been explored for flapping wing mechanisms [26], vibration locomotion [27], a soft pneumatic pump [28] and a soft gripper with fast release mechanism [29].

Despite the potential for DEAs to generate mimetic actuation within artificial musculoskeletal robotic systems, the inherent elasticity of DEAs for energy efficient bio-inspired robotics has not been widely

studied. In this work, we seek to investigate the feasibility of DEAs as an analogue to the energy capture-and-release characteristics of the natural muscle-tendon complex towards increasingly lightweight and energy-efficient bio-inspired robotics. In our previous initial work [30], by adopting the double cone configuration, we have demonstrated the feasibility of recovering the elastic energy stored in DEA membranes. However, in that work, only primitive experimental results were shown with no analysis on the principle itself. Here, we use the same DEA design to conduct in-depth performance analyses of the double cone DEA (DCDEA) design and its inherent elastic energy recovery to demonstrate the feasibility of using this DEA design in bio-inspired robotics. The key contributions of this paper include: (i) developing a complete electromechanical model to characterize the dynamic performance of the DCDEA; (ii) conducting a comprehensive analysis on the power/stroke output and its electromechanical response against various payload conditions; (iii) comparing the effects of actuation signal waveforms on output performance of the DCDEA; (iv) proposing a novel elastic energy recovery scheme for antagonistic DEA actuations and demonstrating the same principle using a bioinspired leg demonstrator.

The rest of this paper is structured as follows: in Section II, the DCDEA design is presented and a mathematical model is developed to characterize its dynamic performance. In Section 3, the proposed model is validated against experimental results and the DCDEA configuration is optimized based on this model to maximize its work output. Using this numerical model and the optimized design, in Section 4, we present a comprehensive study on both the power and stroke outputs and the electromechanical efficiency of the DCDEA using a DEA-mass-dashpot system. In Section 5, a bio-inspired robotic leg design powered by the DCDEA is presented and demonstrations are presented with the focus on the inherent compliance and elastic energy recovery of the DEA. Finally, in Section 6, conclusions are drawn, and future work is discussed.

2. DCDEA dynamic electromechanical model

2.1 DCDEA design overview

A cone DEA design consists of an elastomer membrane bonded to a circular frame with a protrusion pushing the centre of the membrane to form a cone shape. The protrusion force can be exerted from a compression spring [31], a deadweight [32] [33] [34], a bistable mechanism [35] [32], magnetic attraction [36] [37] [38] or repulsion [39], or a counter force from another cone DEA through a rigid strut [9] [40]. In this work, a double cone design is adopted for its natural agonist-antagonist configuration as the two single conical DEA membranes can be actuated separately to produce bidirectional actuation, thus mimicking the typical agonist-antagonist muscle and tendon system.

Figure 1 (**a**) illustrates a schematic diagram of the DCDEA design, which consists of two dielectric elastomer membranes bonded to circular frames and the centre of the membranes are protruded by a rod. Compliant electrodes are coated on two sides of the membranes to enable actuation. A fabricated DCDEA is shown in **Figure 1** (**b**).

2.2 DCDEA model development

Several cone DEA models have been proposed, for example, a quasi-static model based on the thermodynamic equilibrium and geometric relationships [41]. This model can capture the non-truncated membrane shape (as shown in **Figure 1** (**b**)) and concomitant inhomogeneous stress distribution. The viscoelastic behaviour of a conical DEA has been investigated in [42] [43] by including time-dependent viscosity into this model. However, such model has the significant drawback of heavy computational cost because of the shooting method used in the numerical method to solve a set of partial differential equations and algebraic equation to meet the boundary conditions [44]. This computationally intensive model makes it challenging to predict the dynamic responses of a conical DEA with the constantly changing actuation voltage and boundary conditions (e.g. force, displacement). To cope with this issue, a commonly used cone DEA model assumes a truncated cone shape (as illustrated by the red dash lines in **Figure 1** (**b**)) and a homogeneous stress distribution on the deformed DEA membrane, as adopted in [21] [33] [45] [46] [47] [48] [49]. This model significantly reduces the computational cost for dynamic modelling and has been widely verified against experimental results. For these reasons, the proposed dynamic DCDEA model in this work is developed based on the same assumption of a truncated cone shape.

2.2.1 Mechanical model

This subsection describes the mechanical model of the DCDEA. Frist, the following simplifying assumptions are defined: (**i**) this is a single degree-of-freedom system, i.e. only translation along the vertical axis is modelled here (note that this actuator can have 6 DOF, see [10] for example, however, we restrict our focus on the vertical translation to avoid overcomplicate the modelling); (**ii**) truncated conical deformation; (**iii**) homogenous strain distribution on the membrane; (**iv**) the circumferential deformation of the membrane does not vary.

The schematic diagram of the DCDEA model is illustrated in **Figure 2**. First, a piece of elastomer with the initial thickness of H_0 is pre-stretched biaxially by $\lambda_p \times \lambda_p$ and is constrained to a ring with an inner radius, b, and a central disk with an outer radius, a. Then a rod is added to the centre of two pre-stretched membranes, forcing an out-of-plane deformation on each membrane by $L/2$ and an angle is formed

between the membrane and the horizontal plane by θ_I and θ_{II}, respectively. The tension of the membranes results in forces, F_{DEA_I} and F_{DEA_II}, on the rod along the vertical axis. As an electric field is applied across the top membrane, the rod along with the two membranes move upward, the stroke, d, is measured with reference to its passive position. The radial stretch of the top and bottom membranes, λ_{i_1} (i = I, II for top and bottom respectively), at an arbitrary stroke, d, can be defined as

$$\lambda_{I\_1} = \frac{\sqrt{(L/2+d)^2+(b-a)^2}}{(b-a)}\lambda_p \,, \tag{1}$$

$$\lambda_{II\_1} = \frac{\sqrt{(L/2-d)^2+(b-a)^2}}{(b-a)}\lambda_p \,. \tag{2}$$

(Note that an upward stroke results in a positive d value while a downwards stroke leads to a negative d.)

By assuming the material is incompressible (i.e. the principle stretches $\lambda_1\lambda_2\lambda_3 = 1$), the thickness of the two membranes in its deformed state can be described as

$$H_i = \frac{H_0}{\lambda_{i\_1}\lambda_{i\_2}} \,. \tag{3}$$

The angles between the membranes and the horizontal plane, θ_I and θ_{II}, can be expressed as

$$\sin\theta_I = \frac{L/2+d}{\sqrt{d^2+(b-a)^2}}, \tag{4}$$

$$\sin\theta_{II} = \frac{L/2-d}{\sqrt{d^2+(b-a)^2}} \,. \tag{5}$$

During actuation, the inertia and the gravitational force of the rod is balanced by the net force of the two membranes, as expressed as follows

$$mg + m\ddot{d} = -F_{DEA\_I} + F_{DEA\_II} \,, \tag{6}$$

where m is the mass of the rod (and any payload connected to the rod) and the negative sign before F_{DEA_I} indicating a force pointing downwards.

The forces that the two membranes exert can be described as

$$F_{DEA\_i} = 2\pi a H_i \, \sigma_{i\_1} \sin\theta_i \,, \tag{7}$$

where σ_{i_1} (i = I, II) is the radial stresses of the two membranes respectively.

In this work, the Ogden model [50] is adopted to describe this strain-stress relationship and, to take viscoelasticity into account (including viscous damping and creep phenomenon as commonly observed in the commonly used 3M VHB 4905/4910 dielectric material), a rheological material model with parallel Kelvin-Voigt and Maxwell models [51] is proposed, as illustrated in **Figure 3**. On the first branch is the Ogden spring that describes the hyperelasticity of this material, on the middle branch is a spring in series with a dashpot which mainly represents the creep phenomenon. To cope with the significant viscosity of VHB material, a dashpot is included in the last branch to characterize the viscosity. Note that for the spring on the first unit, its deformation is characterized by λ_1 and λ_2. However, for the spring in the second unit, its deformation is characterized by λ_1^e and λ_2^e due to the dashpot. Let ξ_1 and ξ_2 be the stretches of the dashpot and because the two units have the same net stretches, λ_1 and λ_2, the stretches for spring 2 can be written as

$$\lambda_1^e = \frac{\lambda_1}{\xi_1}, \lambda_2^e = \frac{\lambda_2}{\xi_2}. \tag{8}$$

The total radial stress of the material can be represented by the summation of the stresses from the three parallel units, as written as

$$\sigma_{i\_1} = \mu_1\left(\lambda_{i\_1}^{\alpha_1} - \lambda_{i\_1}^{-\alpha_1}\lambda_{i\_2}^{-\alpha_1}\right) + \mu_2\left(\lambda_{i\_1}^{\alpha_2} - \lambda_{i\_1}^{-\alpha_2}\lambda_{i\_2}^{-\alpha_2}\right) - \varepsilon_0\varepsilon_r E_i^2 + \mu_3\left({\lambda_{i\_1}^e}^{\alpha_3} - {\lambda_{i\_1}^e}^{-\alpha_3}{\lambda_{i\_2}^e}^{-\alpha_3}\right) + \eta_2\frac{\dot{\lambda}_{i\_1}}{\lambda_{i\_1}}, \tag{9}$$

where $\mu_{1,2,3}$ are shear moduli, $\alpha_{1,2,3}$ are power constants, $\eta_{1,2}$ are the damping coefficients, ε_0 and ε_r are the absolute permittivity of a vacuum and the relative permittivity of the dielectric elastomer respectively, E_i (i = I, II) is the applied electric field of the two membranes and is given as $E = \Phi_{DEA}/H$, with voltage across the DEA membrane, Φ_{DEA}, and membrane thickness, H.

By modelling the dashpot as a Newtonian fluid [52], the rate of deformation of the dashpot in equation (8) can be described as

$$\frac{d\xi_{i\_1}}{dt} = \frac{\xi_{i\_1}}{3\eta_1}\left(\mu_3\left({\lambda_{i\_1}^e}^2 - {\lambda_{i\_1}^e}^{-2}{\lambda_{i\_2}^e}^{-2}\right) - \mu_3\left({\lambda_{i\_2}^e}^2 - {\lambda_{i\_1}^e}^{-2}{\lambda_{i\_2}^e}^{-2}\right)/2\right), \tag{10}$$

$$\frac{d\xi_{i\_2}}{dt} = \frac{\xi_{i\_2}}{3\eta_1}\left(\mu_3\left({\lambda_{i\_2}^e}^2 - {\lambda_{i\_1}^e}^{-2}{\lambda_{i\_2}^e}^{-2}\right) - \mu_3\left({\lambda_{i\_1}^e}^2 - {\lambda_{i\_1}^e}^{-2}{\lambda_{i\_2}^e}^{-2}\right)/2\right). \tag{11}$$

Based on the assumption that the circumferential strain remains unchanged in this system, $\lambda_{i\_2}^e = 1$. If the voltage Φ_{DEA} is known, then by substituting (9 and 10) into (7), the DEA force can be calculated

and by solving the ordinary differential equation (6) numerically, the dynamic response of a DCDEA can be estimated. In the following subsection, we develop the electrical model that estimate Φ_{DEA} as a function of time with a given voltage input, Φ_{in}.

2.2.2 Electrical model

Electrically, a DEA can be considered as a deformable capacitor, C, in series with a resistor, R_s, representing the surface resistance of the compliant electrodes and the connection between the high voltage supply [52]. For ideal capacitors, no current flows through the capacitors at any time when a DC voltage is applied across. However, real capacitors have a leakage current, as a result, a parallel resistor, R_l, is added to this model to capture this phenomenon. A schematic diagram of this electrical model is illustrated in **Figure 4**. The total current flow in the system can be described as

$$i = \dot{Q} + i_{leak} \, , \tag{12}$$

where i is the total current, $\dot{Q}$ is the rate of change of the polarizing charge accumulated on the DEA and i_{leak} is the current leaking through the DEA.

When a voltage Φ_{in} is applied by the high voltage supply, charge flows into the DEA, and rate of charge and voltage across the DEA membrane can be expressed as

$$\dot{Q} = -\frac{1}{R_s C} Q + \frac{1}{R_l} \Phi_{in} \, , \tag{13}$$

$$\Phi_{DEA} = \frac{1}{C} Q \, . \tag{14}$$

Note that despite the fact that R_s and C can vary during actuation (due to the membrane deformation), here we assume these parameters remain constant during actuation as the stroke is usually one order of magnitude smaller than the rod height which causes the out-of-plane deformation, so it is safe to assume that these values are dominated by the pre-stretch and initial out-of-plane deformation and the actuation stroke has negligible effect on these values.

The leakage current through polymers has been proven to be a complex phenomenon which is affected by several factors such as molecular configuration, impurities, temperature and humidity [52]. In this work we adopt an exponential function from [52] where the density of the leakage current is written as

$$j_{leak} = \gamma E e^{E/E_b} \, , \tag{15}$$

where γ is the conductivity at low field, and E_b is a constant with the unit of electric field.

The leakage current can be expressed as

$$i_{leak} = j_{leak}\pi(b^2 - a^2)\cos\theta \ . \quad (16)$$

By substituting (15 and 16) into (12) and solving the ordinary differential equation (13) numerically, the voltage Φ_{DEA} and current i as a function of time can be estimated. With these values known, the dynamic response of the DCDEA can be described together with the mechanical model developed in the last subsection.

3 DCDEA performance characterization

In this section, the performance of the DCDEA is characterized using both experiments and numerical model, its configuration is optimized in terms of maximum work output and the compliance actuation of the DCDEA is demonstrated.

3.1 DEA fabrication

The fabrication process of the DCDEAs is introduced as follows. For each membrane, a piece of VHB 4905 tape (3M) was biaxially pre-stretched by 3×3 and then bonded to a rigid circular frame with an inner radius of 20 mm. One disk with 5 mm radius was centrally aligned and bonded on the underside of the membrane. Carbon conductive grease (M.G. Chemicals Ltd) was hand brushed onto each side of the membrane as the compliant electrodes. A spacer was attached to each end to protrude the membranes out-of-plane and rigidly couple them together. The two circular frames were then fixed together with nylon fasteners.

3.2 Quasi-static characteristic of a single cone DEA

The measured and modelled quasi-static force-displacement relationship of a single cone DEA is shown in **Figure 5**, where the negative displacement value is due to the downward deformation of the DEA membrane. Detailed experimental setup for quasi-static force-displacement measurement follows the same setup in our previous works [39] [53] and can be found in supplementary material. The quasi-static model parameters (μ_1, μ_2, α_1, α_2) of Ogden model in equation (9) were determined by a least-mean-squared algorithm in MATLAB (following [33] [48]) and the identified values are μ_1 = 47.89 kPa, μ_2 =

10.02 Pa. α_1 = 2.059 and α_2 = 5.306. As can be seen in **Figure 5**, a very good agreement can be found between the measurement and the model prediction. It is also notable that despite the nonlinearity of the strain-stress relationship and the complex three-dimensional geometry, the force-displacement curve of a single cone DEA is close to a linear relationship.

3.3 Quasi-static work output optimization

With the parameters of the Ogden model determined, now a quasi-static DCDEA model can be used to optimize the design variable rod height in terms of the maximum work output of a DCDEA. The maximum work this actuator could exert is simply found by integrating the force-stroke curve: $W_{max} = \int_0^{d_{max}} F_{out}(d)\, dd$, where F_{out} is the output force and d is the stroke. By using the quasi-static model (neglecting the electrical response and the viscoelasticity in the membrane), the maximum work output of the DCDEAs with the rod lengths from 10 to 40 mm were evaluated and the result is shown in **Figure 6** (**a**). A fixed electric field of 80 MV/m was used in this evaluation. As can be seen, the DCDEA has a peak in work output at L = 26 mm and within the range between 20 and 33 mm, the W_{max} remains within a high value range. Based on the optimal work output criteria, L = 26 mm is used in the rest of this work. **Figure 6** (**b**) shows the examples of the force-stroke curves of the DCDEAs with L = 20, 25 and 30 mm. Note that as the rod height increases, the maximum force output increases, while the maximum stroke reduces. This suggests that apart from the optimal work output, the rod height can be selected based on the specific applications where either a higher force or a longer stroke is desired. It is worth noting that in this optimization, only one membrane was actuated. For DCDEAs where two membranes can be actuated antagonistically, the total work output can be doubled.

3.4 DCDEA dynamic characterization

The dynamic performance of a DCDEA was evaluated by applying two alternating current voltages across the top and bottom membranes. Square and sinusoidal waveforms were as a comparison. Experimental setups are described in detail in supplementary material.

The measured strokes and the model predicted results under square and sine waves with different voltage amplitudes and frequencies are shown in **Figure 7**. The dynamic model parameters were determined by the same least-error principle as above with varying actuation voltage amplitudes and frequencies. The identified values are μ_3 = 80 kPa, η_1 = 80 kPa·s, η_2 = 199.1 kPa·s. α_3 = 2 is manually defined. The model prediction agrees very well with experimental results for both square and sine waves. Note that at a given voltage amplitude and frequency, the square wave can result in a larger stroke than sinusoidal wave. Due to the high viscosity of the VHB material, the stroke reduces gradually

with the increasing frequency. **Figure 8** shows the time series of the dynamic response of the DCDEA with a square and sinusoidal actuation wave. Again, the model matches very well with the measurement. Note that the DCDEA is clearly an overdamped system as there is no overshoot in the step response.

The measured and modelled current flow in the top DEA membrane are also shown in **Figure 8**. The model parameters were determined as: R_s = 35 MΩ, $\gamma = 7\times10^{-14}$ S/m, E_b = 20 MV/m and the capacitance was measured at C = 0.9 pF using a high-precision LCR meter (E4980AL, Keysight). It can be seen that the electrical model captures the charging and discharging current flows accurately. Note that the peak current flow in a square wave actuation is over one order of magnitude higher than the sinusoidal waves, which suggests a significantly higher peak power demand for the square wave. **Figure 9** shows a close comparison of the measured and simulated charging current, i_1, as a function of time in a square wave actuation. Both the experimental result and the model simulation show that the current is greater than zero after the DCDEA is charged. This leakage current results in an energy loss when the DEA reaches a steady state and is maintaining a position. This energy loss needs to be taken into account in any practical applications of DEAs.

3.5 Complaint actuation of DCDEA

The inherent compliance of the DCDEA can offer an advantage over other actuators since it can still function even it is initially deformed by an external force. In this subsection, the dynamic performance of the DCDEA is further investigated against the deformation of the actuator by letting the DCDEA drive a mass against gravity, as shown in **Figure 10** (**a**). With a mass attached to the actuator, the balancing position of the DCDEA will be lower than its reference position, as illustrated in **Figure 10** (**a**). In **Figure 10** (**b**), a clear difference can be noticed in the DCDEA position with and without a 40 g mass attached. **Figure 10** (**c**-**d**) shows the measured and modelled performance of the DEA as a function of mass respectively. It can be seen that as the mass becomes heavier, the balancing position of the DEA becomes lower, the upward stroke becomes smaller while the downward stroke increases. However, the total stroke (the difference between the top (red curve) and bottom (green curve) positions) remains approximately unchanged, which suggests that despite the balancing position of the DCDEA changing with the payload due to its inherent compliance, its actuation performance remains stable. This is particularly important for applications such as dynamic locomotion where the balancing position of the actuator is constantly changing due to the dynamic motion.

4. Energetic study of DCDEA

In the last section, the proposed dynamic model was compared with the experimental results with excellent accuracy. The DCDEA configuration was optimized in terms of work output in a quasi-static actuation. However, in applications such as robotic locomotion, the power output and the energy efficiency of the actuator are also critical. In this section, this model is utilized to perform an energetic study of the DCDEA which investigates the power and stroke output of the DCDEA and the electro-mechanical efficiency of the DCDEA. A novel strategy of utilizing the inherent elastic energy stored in the DEA membranes is also demonstrated.

4.1 Energetic study definition

This study focuses on a simple system where a DCDEA drives an inertial and dispersive payload, as illustrated in **Figure 11**. The DCDEA drives the mass, *M*, to move horizontally and the mass is also rigidly connected to a dashpot with the damping coefficient, *c*. The dashpot always absorbs energy, resulting in a positive work output from the DCDEA in one cycle. In this study, the same DCDEA configuration from the preceding section was adopted (a = 5 mm, b = 20 mm, L = 26 mm). The mass, *M*, was fixed at 10 g. Here we investigate the energetic performance of the DCDEA with varying actuation frequencies and damping coefficients representing different applications. The square and sinusoidal actuation signals with alternating current and amplitude of 3 kV were used with the frequencies varying from 0.1 to 10 Hz. The damping coefficient, *c*, was varied from 0.1 to 100 N.s/m.

Before conducting the study, the following parameters are defined.

The work output of the DCDEA in one cycle is

$$W_{out} = \int_0^T cv^2\, dt\,, \tag{17}$$

where T is the period, v is the velocity, t is time.

The electrical energy input of the DCDEA in one cycle is

$$E_{in} = \int_0^T \phi_{in}(t) i(t)\, dt\,. \tag{18}$$

Note that in this study, we assume there is no electrical energy recovery, i.e. current flowing back into the power supply ($i(t) < 0$) is not considered.

The average power output of the DCDEA is

$$P_{out} = \frac{W_{out}}{T}\,, \tag{19}$$

and the electromechanical efficiency is

$$\eta_{em} = \frac{W_{out}}{E_{in}}\,. \tag{20}$$

In this system, during actuation, the kinetic energy of the mass, E_k, and the elastic stain energy of the DCDEA membranes, E_s, also fluctuate in one cycle, which are written as

$$E_k = \frac{1}{2}Mv^2\,, \tag{21}$$

$$E_s = W_s Vol\,, \tag{22}$$

where the strain energy density is given in Ogden model as

$$W_s = \sum_{i=1}^{2}\left(\frac{\mu_1}{2}\left(\lambda_{i\_1}^2 + \lambda_{i\_2}^2 + \lambda_{i\_1}^{-2}\lambda_{i\_2}^{-2} - 3\right) + \frac{\mu_2}{4}\left(\lambda_{i\_1}^4 + \lambda_{i\_2}^4 + \lambda_{i\_1}^{-4}\lambda_{i\_2}^{-4} - 3\right)\right), \tag{23}$$

and the volume of the membrane is

$$Vol = \pi(b^2 - a^2)\frac{H_0}{\lambda_p^2}\,. \tag{24}$$

4.2 Energetic study findings

The power output of the DCDEA as a function of the damping coefficient and the actuation frequency is shown in **Figure 12**. By comparing the square wave and sinusoidal wave results, it can be noted that square actuation signals result in higher average power outputs. For this DCDEA design, the maximum power output that can be achieved is about 0.4 mW at a frequency of 1 Hz using a square wave signal. The red curves in **Figure 12** show the frequency which generates the peak power output for each damping coefficient values. Note that for both square and sinusoidal waves, as the damping coefficient increases, the maximum power output occurs at a lower frequency but all within the frequency range of 0.5 to 2 Hz. **Figure 13** compares the power output as a function of damping coefficients with the frequency fixed at 1 Hz. The power output increases with the increasing damping coefficient and peaks at c = 20 N.s/m for both square and sinusoidal waves, as c increases further, P_{out} reduces gradually. It is worth noting that the power output with a square wave is almost twice that with a sinusoidal wave.

Figure 14 shows the stroke output of the DCDEA and it can be noted that the square wave results in a larger stroke than the sinusoidal wave in all cases. At an extremely low frequency (e.g. f = 0.1 Hz), the stroke remains a constant value regardless of the damping coefficient. However, as the actuation frequency and damping coefficient increases, the stroke drops gradually. It is worth noting that when c < 10 N.s/m, the stroke is dominated by the actuation frequency, and at 10 Hz, the stroke is close to zero even when the damping from the payload is negligible, which demonstrates that the substantial viscosity in the DEA itself restricts the application of the VHB based DCDEA at high frequencies.

Another parameter that describes the energetic characteristic of a DEA is its electromechanical efficiency. **Figure 15** compares the electromechanical efficiency of the DCDEA with square and sinusoidal actuation signals. It can be noticed that the highest efficiency occurs at the lowest frequency of 0.1 Hz and the highest damping coefficient of 100 N.s/m, which could be due to the low actuation frequency resulting in a larger stroke, and hence a greater work output, and the high damping coefficient, c, leading to a slower velocity and a lower viscous loss in the DEA, i.e. a higher proportion of velocity-dependent dissipation is lost to the load rather than within the membrane. As illustrated by the red curves, as c reduces, the maximum electromechanical efficiency occurs at a higher frequency but with a reducing value.

The key findings of this energetic study can be summarized as follows: (**i**) DCDEAs with square wave actuation signals have a better overall performance than sinusoidal wave; (**ii**) the significant viscosity of the VHB material limits the bandwidth of this DCDEA design within 10 Hz and if the maximum power output is desired, the frequency should be restricted to less than 2 Hz; (**iii**) without electrical energy recovery, the electromechanical efficiency of a DCDEA is less than 4%, but if electrical energy recovery is allowed by the high voltage power supply then this efficiency can be higher. It is worth pointing out that this study only considers the relatively simple case of a DCDEA driving a mass and a dashpot and, as a result, these findings may not be conclusive for other types of applications.

4.3 Utilizing the inherent elasticity in DEA for work output

The inherent elasticity of the membrane means that DEAs differ from most types of conventional actuator in terms of elastic energy storage as no additional elastic element is required in a DEA to store and release elastic energy. **Figure 16** shows the elastic strain energy fluctuation of the DCDEA in one actuation cycle. It can be seen that the elastic strain energy increases as the DEA is generating stroke (moving towards each end) and reduces as the DEA returns to its balance position (d = 0). Note that the kinetic energy of the mass, E_K, also fluctuates during one cycle, however, its values is found to be three orders of magnitude smaller than the change in the elastic strain energy, hence it is not studied here.

To take advantage of the elastic strain energy fluctuation, the duty ratio (*DR*) of the two square actuation signals can be reduced such that a period is left passive after the elastic strain energy reaches its peak value and, during this passive period, this energy is released so that part of it is converted to the work output (driving the mass and dashpot). An example of this concept is illustrated in **Figure 17**. In this example, the duty ratio of the two signals are reduced from 0.5 to 0.3, so that a 0.2 s period is left passive after each DEA membrane is switched off. During this 0.2 s period, the DEA is driven by the elastic strain energy stored in its membranes towards its reference position, continuously outputting work without any electrical energy input. After this passive period, the DEA is switched on again, and the elastic strain energy is charged as part of the actuation process. **Figure 18** compares the contribution of the elastic strain energy in the work output in one complete cycle as a function of the duty cycle. As can be seen, a greater percentage of work is done during the passive period as the duty ratio reduces and about 28% of the total work output is contributed by the elastic strain energy stored in the DEA membranes during the passive period when *DR* is reduced to 0.2. However, it is worth noting that the total work output reduces as the duty ratio becomes smaller due to the lower electrical energy input. This elastic energy recovery concept can be explored further in applications such as bio-inspired locomotion where elastic energy recovery can used to improve the energy efficiency.

5. Bio-inspired robotic application demonstration

In Section 3, the DCDEA was demonstrated to have beneficial compliance where its actuation performance showed negligible dependence on the deformation of its balancing position. In Section 4, we demonstrated that the inherent elastic energy stored in the DEA membranes can recovered to produce work output. In this section, to demonstrate the feasibility of utilizing double cone DEAs for bio-inspired robotics, we present a leg design powered by DCDEAs to showcase the advantage of the compliance and elastic energy recovery of the DCDEA.

5.1 DCDEA-driven robotic leg demonstrations

The proposed bio-inspired robotic leg is shown in **Figure 19**. The leg design is a biologically inspired three-segment configuration, which is commonly seen in the hind limbs in mammals [1] and has been adopted in quadrupedal robot designs such as BigDog [3], Puppy II [4], Cheetah-cub [5]. The detailed design parameters and the fabrication process of this leg design is given in supplementary material. A kinematic model of the leg design is developed and verified, which can also be found in supplementary material.

Compliant actuation demonstration. In the first demonstration, the DCDEA powers the knee joint and generate a squat motion. **Figure 20** (**a-b**) shows that the leg does squat with its bodyweight and with 5 g mass attached respectively. The 5 g mass caused the leg to lower its position and the DCDEA was

deformed further from its initial position. However, the DEA was still functioning and driving the leg together with the payload down and upwards thanks to the inherent compliance of the DEA.

Elastic energy recovery demonstration. In the second demonstration, the same squat motion was repeated, but with a reduced duty ratio in the actuation signals to demonstrate its elastic energy recovery. **Figure 21** shows the snapshots of the leg in actuation and the time series of the two actuation signals, change in knee angles and the fluctuation in the elastic strain energy in the DEA membranes in one cycle with the period of 2 s. In the first second, voltage Φ_I is on, which causes the DEA to lower the leg, and the elastic strain energy in the antagonistically coupled membranes is increased in this process. Between t = 1 – 1.2 s, both voltage signals are off, and the increment in the elastic strain energy in the first second is released, causing the leg to lift up. The passive release of stored strain energy in this period generates a knee joint stroke of 6.5˚, which highlights the benefits of taking inspiration from principles of biological legged locomotion (where the natural muscle-tendon complex performs a similar function [1]). Note that the leg does not entirely return to its initial passive position in this 0.2 s, which could be due to the friction in the joint and the viscoelasticity of the DEA. During t = 1.2 to 2 s, the Φ_{II} is turned on, which forces the leg to stand up and drive the knee joint through a further 11.5˚. The total stroke of the knee joint in one cycle is 18˚ with a reduced duty ratio in the actuation signals.

5.2 Discussion

The proposed leg design demonstrated the capability of compliant actuation and elastic energy recovery using only the inherently elastic actuator. The promising results offer potential opportunity in utilizing this elastic actuator in bio-inspired or biomimetic robots with inherently compliant actuation units and elastic energy recovery capabilities.

In the current DCDEA design, VHB 4905 material was adopted for its relatively high dielectric constant (~ 4.7) and high dielectric strength (>120 MV/m [7]), which allowed a large stroke/work output at low frequencies, as was shown in Section 4. A comparison of the quasi-static force-stroke output of VHB DCDEA and a silicone DCDEA is available in Figure S6 in supplementary material. However, the large viscosity of this material limits the bandwidth of the DCDEA to be less than 10 Hz. Silicone elastomers, on the other hand, despite having a relatively low dielectric constant (~ 2.7 [54]) and low dielectric strength (~ 80 – 100 MV/m [54]), offer significantly lower viscosity which enables the DEAs to have a peak stroke/work output at a higher frequency, as has been demonstrated before [26] [29] [33]. As a result, DEA materials can be chosen for specific applications where the optimal actuation frequency of the DEA lies within the application requirements.

6 Conclusion

To summarize, in this work, by adopting a double cone DEA configuration, we conducted a compressive study in the dynamic performance of the double cone DEA using both an experimental approach and analytical modelling. The key findings are list as follows:

i. The configuration of the double cone DEA was optimized in terms of work output and the optimal configuration found was to be a 1.3 height-to-radius ratio.

ii. By using a DEA-mass-dashpot system, square wave actuation signals were found to lead to a higher power output with a better electromechanical efficiency than sinusoidal wave signals.

iii. The double cone DEA made with VHB material has a peak power output at a frequency between 0.5 to 2 Hz and the actuation bandwidth of this DEA was found to be less than 10 Hz due to the inherent viscosity of the material.

iv. Inherent elastic strain energy stored in the DEA membranes can be recovered by reducing the duty ratio of the actuation signals thus allowing the released elastic strain energy to contribute to the work output.

With the optimal double cone DEA configuration, we developed a bio-inspired robotic leg with the double cone DEAs as a demonstrator to prove the feasibility of utilizing the compliant actuation and elastic energy recovery for bio-inspired or biomimetic robotics. The electromechanical dynamic model of double cone DEAs developed in this work can be a useful tool for performance characterization and optimization in other bio-inspired applications such as flapping wing robots or jumping robots.

Acknowledgement

C. Cao appreciates the support from the EPSRC Centre for Doctoral Training in Future Autonomous and Robotic Systems (FARSCOPE) at the Bristol Robotics Laboratory. X. Gao and A. Conn acknowledge support from EPSRC grant EP/P025846/1.

Data statement

Data are available at the University of Bristol data repository, data.bris, at https://doi.org/10.5523/bris.301yc2s14kv2o2v426lrfy5y8f.

References

[1] R. Alexander, "Three uses for springs in legged locomotion," *International Journal of Robotics Research,* vol. 9, no. 2, pp. 53-61, 1990.

[2] C. P. Ellington, "The novel aerodynamics of insect flight: applications to micro-air vehicles," *Journal of Experimental Biology,* vol. 202, no. 23, pp. 3439-3448, 1999.

[3] M. Raibert, K. Blankespoor, G. Nelson and R. Playter, "Bigdog, the rough-terrain quadruped robot," in *IFAC Proceedings Volumes*, 2008.

[4] F. Iida, G. Gómez and R. Pfeifer, "Exploiting body dynamics for controlling a running quadruped robot," in *International Conference on Advanced Robotics*, 2005.

[5] A. Spröwitz, A. Tuleu, M. Vespignani, M. Ajallooeian, E. Badri and A. J. Ijspeert, "Towards dynamic trot gait locomotion: Design, control, and experiments with Cheetah-cub, a compliant quadruped robot," *The International Journal of Robotics Research,* vol. 32, no. 8, pp. 932-950, 2013.

[6] K. Y. Ma, P. Chirarattananon, S. B. Fuller and R. J. Wood, "Controlled flight of a biologically inspired, insect-scale robot," *Science,* vol. 340, no. 6132, pp. 603-607, 2013.

[7] R. Pelrine, R. Kornbluh, Q. Pei and J. Jose Joseph, "High-Speed Electrically Actuated Elastomers with Strain Greater Than 100%," *Science,* pp. 836-839, 2000.

[8] Q. Pei, M. Rosenthal, S. Stanford, H. Prahlad and R. Pelrine, "Multiple-degrees-of-freedom electroelastomer roll actuators," *Smart materials and structures,* vol. 13, no. 5, p. N86, 2004.

[9] H. R. Choi, K. M. Jung, J. W. Kwak, S. W. Lee, H. M. Kim, J. W. Jeon and J. D. Nam, "Digital polymer motor for robotic applications," in *In Robotics and Automation, 2003. Proceedings. ICRA'03. IEEE International Conference on*, 2003.

[10] A. T. Conn and J. Rossiter, "Towards holonomic electro-elastomer actuators with six degrees of freedom," *Smart Materials and Structures,* vol. 21, no. 3, p. p.035012, 2012.

[11] P. Wang and A. T. Conn, "Elastic cube actuator with six degrees of freedom output," *Actuators,* vol. 4, no. 3, pp. 203-216, 2015.

[12] F. Carpi, R. Kornbluh, P. Sommer-Larsen and G. Alici, "Electroactive polymer actuators as artificial muscles: are they ready for bioinspired applications?," *Bioinspiration & biomimetics*, vol. 6, no. 4, p. 045006, 2011.

[13] K. Jung, J. C. Koo, Y. K. Lee and H. R. Choi, "Artificial annelid robot driven by soft actuators," *Bioinspiration & biomimetics*, vol. 2, no. 2, p. S42, 2007.

[14] H. Wang, L. Li, Y. Zhu and W. Yang, "Analysis and application of a rolled dielectric elastomer actuator with two degrees of freedom," *Smart Materials and Structures*, vol. 25, no. 12, p. 125008, 2016.

[15] T. Li, Z. Zou, G. Mao, X. Yang, Y. Liang, C. Li, S. Qu, Z. Suo and W. Yang, "Agile and resilient insect-scale robot," *Soft robotics*, vol. 6, no. 1, pp. 133-141, 2018.

[16] J. Cao, L. Qin, J. Liu, Q. Ren, C. C. Foo, H. Wang, H. P. Lee and J. Zhu, "Untethered soft robot capable of stable locomotion using soft electrostatic actuators," *Extreme Mechanics Letters*, vol. 21, pp. 9-16, 2018.

[17] K. M. Digumarti, C. Cao, J. Guo, A. T. Conn and J. Rossiter, "Multi-directional crawling robot with soft actuators and electroadhesive grippers," in *EEE International Conference on Soft Robotics (RoboSoft)*, 2018.

[18] J. Eckerle, S. Stanford, J. Marlow, R. Schmidt, S. Oh, T. Low and S. V. Shastri, "Biologically inspired hexapedal robot using field-effect electroactive elastomer artificial muscles," in *Smart Structures and Materials 2001: Industrial and Commercial Applications of Smart Structures Technologies*, 2001.

[19] Q. Pei, M. Rosenthal, S. Stanford, H. Prahlad and R. Pelrine, "Multiple-degrees-of-freedom electroelastomer roll actuators," *Smart materials and structures*, vol. 13, no. 5, p. N86, 2004.

[20] C. T. Nguyen, H. Phung, H. Jung, U. Kim, T. D. Nguyen, J. Park, H. Moon, J. C. Koo and H. R. Choi, "Printable monolithic hexapod robot driven by soft actuator," in *In Robotics and Automation (ICRA), 2015 IEEE International Conference on*, 2015.

[21] C. T. Nguyen, H. Phung, T. D. Nguyen, H. Jung and H. R. Choi, "Multiple-degrees-of-freedom dielectric elastomer actuators for soft printable hexapod robot," *Sensors and Actuators A: Physical*, vol. 267, pp. 505-516, 2017.

[22] C. T. Nguyen, H. Phung, P. T. Hoang, T. D. Nguyen, H. Jung and H. R. Choi, "Development of an Insect-Inspired Hexapod Robot Actuated by Soft Actuators," *Journal of Mechanisms and Robotics,* vol. 10, no. 6, p. 061016, 2018.

[23] T. Li, G. Li, Y. Liang, T. Cheng, J. Dai, X. Yang, B. Liu, Z. Zeng, Z. Huang, Y. Luo and T. Xie, "Fast-moving soft electronic fish," *Science Advances,* vol. 3, no. 4, p. 1602045, 2017.

[24] J. Shintake, V. Cacucciolo, H. Shea and D. Floreano, "Soft biomimetic fish robot made of dielectric elastomer actuators," *Soft robotics,* vol. 5, no. 4, pp. 466-474, 2018.

[25] T. Yang, Y. Xiao, Z. Zhang, Y. Liang, G. Li, M. Zhang, S. Li, T. W. Wong, Y. Wang, T. Li and Z. Huang, "A soft artificial muscle driven robot with reinforcement learning," *Scientific reports,* vol. 8, no. 1, p. 14518, 2018.

[26] C. Cao, S. Burgess and A. T. Conn, "Towards a dielectric elastomer resonator driven flapping wing micro air vehicle," *Frontiers in Robotics and AI,* vol. 5, p. 137, 2018.

[27] C. Tang, B. Li, H. Fang, Z. Li and H. Chen, "A speedy, amphibian, robotic cube: Resonance actuation by a dielectric elastomer," *Sensors and Actuators A: Physical,* pp. 1-7, 2018.

[28] C. Cao, X. Gao and A. T. Conn, "A Magnetically Coupled Dielectric Elastomer Pump for Soft Robotics," *Advanced Materials Technologies,* p. 1900128, 2019.

[29] X. Gao, C. Cao, J. Guo and A. T. Conn, "Elastic electroadhesion with rapid release by integrated resonant vibration," *Advanced Materials Technologies,* vol. 4, no. 1, p. 1800378, 2019.

[30] C. Cao and A. T. Conn, "Elastic actuation for legged locomotion," in *Electroactive Polymer Actuators and Devices (EAPAD) 2017,* 2017.

[31] Y. Luan, H. Wang and Y. Zhu, "Design and implementation of cone dielectric elastomer actuator with double-slider mechanism," *Journal of Bionic Engineering,* vol. 7, pp. 212-217, 2010.

[32] M. Hodgins, A. York and S. Seelecke, "Experimental comparison of bias elements for out-of-plane DEAP actuator system," *Smart Materials and Structures,* vol. 22, no. 9, p. 094016, 2013.

[33] G. Rizzello, M. Hodgins, D. Naso, A. York and S. Seelecke, "Dynamic modeling and experimental validation of an annular dielectric elastomer actuator with a biasing mass," *Journal of Vibration and Acoustics,* vol. 137, no. 1, p. 011005, 2015.

[34] C. Zhang, W. Sun, H. Chen, L. Liu, B. Li and D. Li, "Electromechanical deformation of conical dielectric elastomer actuator with hydrogel electrodes," *Journal of Applied Physics,* vol. 119, no. 9, p. 094108, 2016.

[35] M. Follador, M. Cianchetti and B. Mazzolai, "Design of a compact bistable mechanism based on dielectric elastomer actuators," *Meccanica,* vol. 50, no. 11, pp. 2741-2749, 2015.

[36] X. Q. Li, W. B. Li, W. M. Zhang, H. X. Zou, Z. K. Peng and G. Meng, "Magnetic force induced tristability for dielectric elastomer actuators," *Smart Materials and Structures,* vol. 26, no. 10, p. 105007, 2017.

[37] T. Yang, Y. Xiao, Z. Zhang, Y. Liang, G. Li, M. Zhang, S. Li, T. W. Wong, Y. Wang, T. Li and Z. Huang, "A soft artificial muscle driven robot with reinforcement learning," *Scientific reports,* vol. 8, no. 1, p. 14518, 2018.

[38] P. Loew, G. Rizzello and S. Seelecke, "A novel biasing mechanism for circular out-of-plane dielectric actuators based on permanent magnets," *Mechatronics,* vol. 56, pp. 48-57, 2018.

[39] C. Cao, X. Gao and A. T. Conn, "A compliantly coupled dielectric elastomer actuator using magnetic repulsion," *Applied Physics Letters,* vol. 114, no. 1, p. 011904, 2019.

[40] F. Branz and A. Francesconi, "Modelling and control of double-cone dielectric elastomer actuator," *Smart Materials and Structures,* vol. 25, no. 9, p. 095040, 2016.

[41] T. He, L. Cui, C. Chen and Z. Suo, "Nonlinear deformation analysis of a dielectric elastomer membrane–spring system," *Smart Materials and Structures,* vol. 8, no. 19, p. 085017, 2010.

[42] B. Wang, Z. Wang and T. He, "Investigation on the viscoelastic behaviors of a circular dielectric elastomer membrane undergoing large deformation," *AIP Advances,* vol. 12, no. 6, p. 125127, 2016.

[43] H. Wang, "Viscoelastic analysis of a spring-connected dielectric elastomer actuator undergoing large inhomogeneous deformation," *International Journal of Mechanical Sciences,* no. 136, pp. 17-23, 2018.

[44] C. Cao and A. Conn, "Performance Optimization of a Conical Dielectric Elastomer Actuator," *Actuators,* vol. 7, no. 2, p. 32, 2018.

[45] M. Hodgins, G. Rizzello, D. Naso, A. York and S. Seelecke, "An electro-mechanically coupled model for the dynamic behavior of a dielectric electro-active polymer actuator," *Smart Materials and Structures,* vol. 23, no. 10, p. 104006, 2014.

[46] G. Rizzello, M. Hodgins, D. Naso, A. York and S. Seelecke, "Dynamic modeling and experimental validation of an annular dielectric elastomer actuator with a biasing mass," *Journal of Vibration and Acoustics,* vol. 137, no. 1, p. 011005, 2015.

[47] A. T. Conn, M. J. Pearson, A. G. Pipe, J. Welsby and J. Rossiter, "Dielectric elastomer vibrissal system for active tactile sensing," in *In Electroactive Polymer Actuators and Devices (EAPAD) 2012*, 2012.

[48] G. Rizzello, M. Hodgins, D. Naso, A. York and S. Seelecke, "Modeling of the effects of the electrical dynamics on the electromechanical response of a DEAP circular actuator with a mass–spring load," *Smart Materials and Structures,* vol. 24, no. 9, p. 094003, 2015.

[49] G. Berselli, R. Vertechy, G. Vassura and V. Parenti-Castelli, "Optimal synthesis of conically shaped dielectric elastomer linear actuators: Design methodology and experimental validation," *IEEE/ASME Transactions on Mechatronics,* vol. 1, no. 67-79, p. 16, 2010.

[50] R. W. Ogden, "Large deformation isotropic elasticity–on the correlation of theory and experiment for incompressible rubberlike solids," *Proceedings of the Royal Society of London. A. Mathematical and Physical Sciences,* vol. 326, no. 1567, pp. 565-584, 1972.

[51] J. Zhang, J. Ru, H. Chen, D. Li and J. Lu, "Viscoelastic creep and relaxation of dielectric elastomers characterized by a Kelvin-Voigt-Maxwell model," *Applied Physics Letters,* vol. 110, no. 4, p. 044104, 2017.

[52] C. C. Foo, S. Cai, S. J. Adrian Koh, S. Bauer and Z. Suo, "Model of dissipative dielectric elastomers," *Journal of Applied Physics,* vol. 111, no. 3, p. 034102, 2012.

[53] C. Cao, T. L. Hill and A. T. Conn, "On the nonlinear dynamics of a circular dielectric elastomer oscillator," *Smart Materials and Structures,* 2019.

[54] S. Rosset, O. A. Araromi and H. R. Shea, "Maximizing the displacement of compact planar dielectric elastomer actuators," *Extreme Mechanics Letters,* vol. 3, pp. 72-81, 2015.

[55] R. M. Alexander and A. Vernon, "The mechanics of hopping by kangaroos (Macropodidae)," *Journal of Zoology*, vol. 177, no. 2, pp. 265-303, 1975.

[56] C. T. Nguyen, H. Phung, T. D. Nguyen, C. Lee, U. Kim, D. Lee, H. Moon, J. Koo and H. R. Choi, "A small biomimetic quadruped robot driven by multistacked dielectric elastomer actuators," *Smart Materials and Structures*, vol. 23, no. 6, p. 065005, 2014.

[57] F. Carpi, P. Chiarelli, A. Mazzoldi and D. De Rossi, "Electromechanical characterisation of dielectric elastomer planar actuators: comparative evaluation of different electrode materials and different counterloads," *Sensors and Actuators A: Physical*, vol. 107, no. 1, pp. 85-95, 2003.

[58] M. Wissler and E. Mazza, "Modeling and simulation of dielectric elastomer actuators," *Smart Materials and structures*, vol. 14, no. 6, p. 1396, 2005.

[59] M. Wissler and E. Mazza, " Mechanical behavior of an acrylic elastomer used in dielectric elastomer actuators," *Sensors and Actuators A: Physical*, vol. 134, no. 2, pp. 494-504, 2007.

Figures

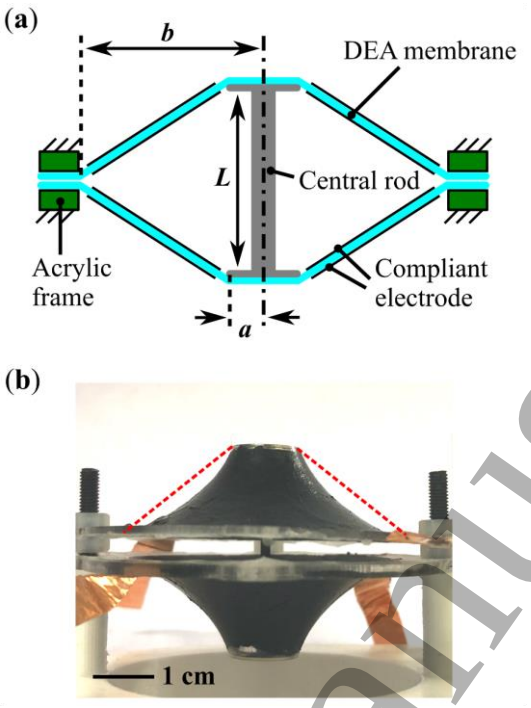

Figure 1. (**a**) Schematic diagram of the DCDEA design. (**b**) Photo of a fabricated DCDEA.

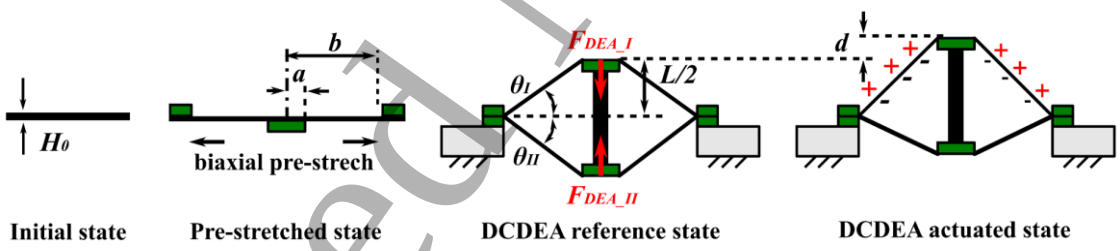

Figure 2. Schematic diagram of the DCDEA mechanical model.

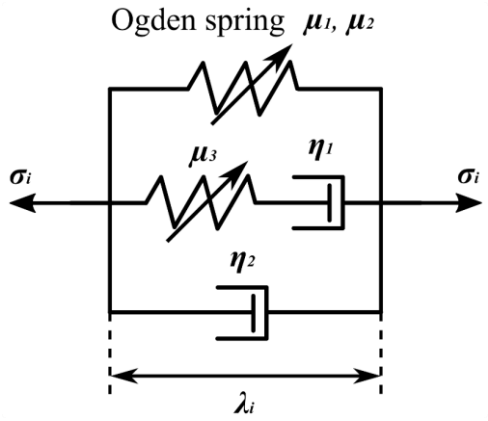

Figure 3. Proposed material model, which consists of three parallel units including a nonlinear hyperelastic spring, a spring in series with a dashpot and a single dashpot.

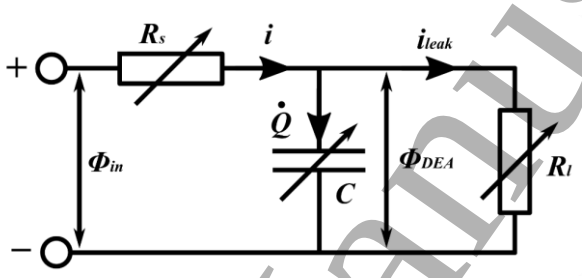

Figure 4. Schematic diagram of the electrical model of the DEA (after [52]).

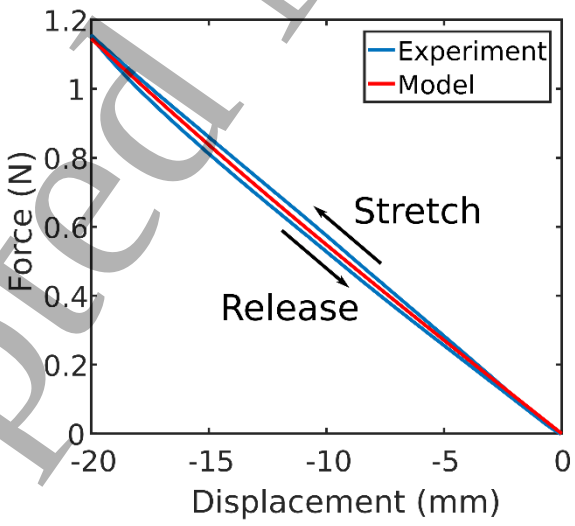

Figure 5. Single cone DEA experimental result and model prediction. The membrane is deformed out-of-plane by 20 mm at the velocity of 0.01 mm/s and then released.

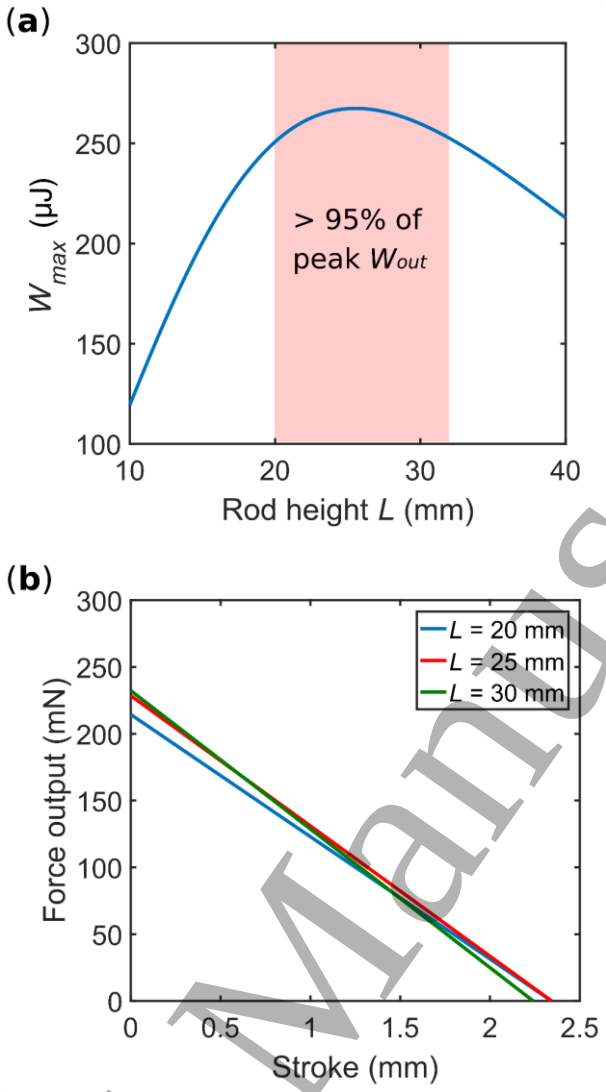

Figure 6. (**a**) Comparison of the maximum work output from the DCDEAs with different rod heights. An optimal rod height is found at 26 mm which generates the maximum work output. (**b**) Examples of the force-stroke output relationships of the DCDEAs with L = 20, 25, 30 mm.

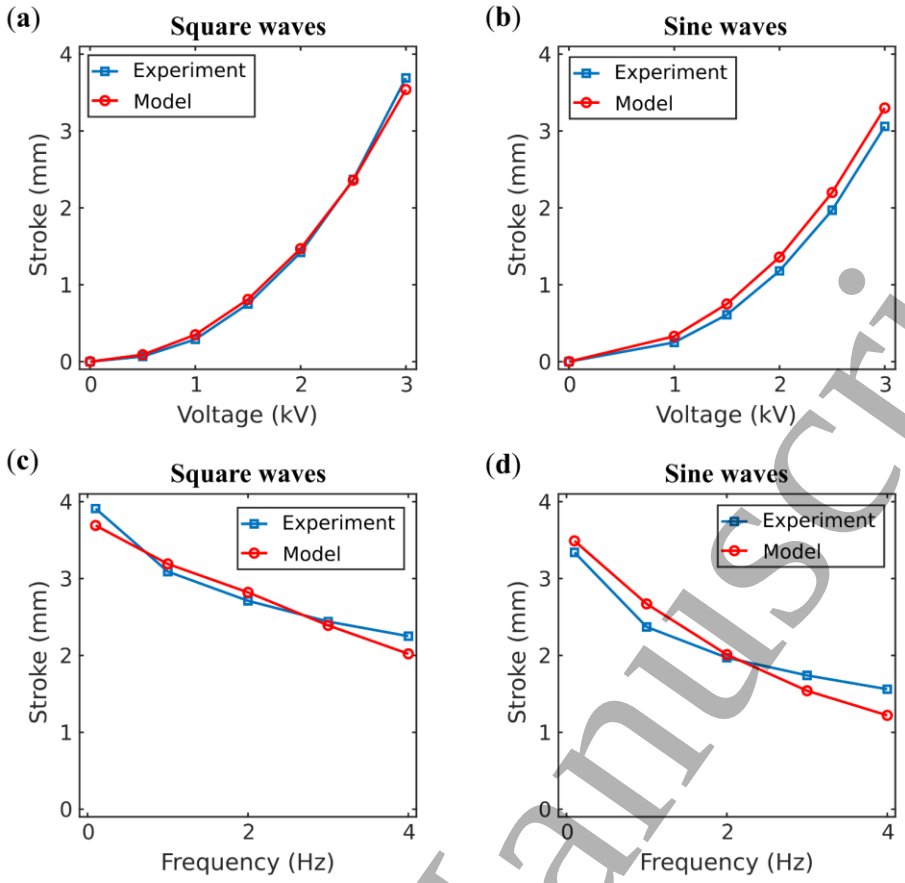

Figure 7. Validation of DCDEA model. Maximum stroke (bi-directional peak-to-peak) of the DCDEA against voltage amplitude of (**a**) square waves and (**b**) sinusoid waves (f = 0.25 Hz). Maximum stroke of the DCDEA as a function of actuation frequency of (**a**) square waves and (**b**) sinusoidal waves (Φ = 3 kV). No payload is included in this set of studies.

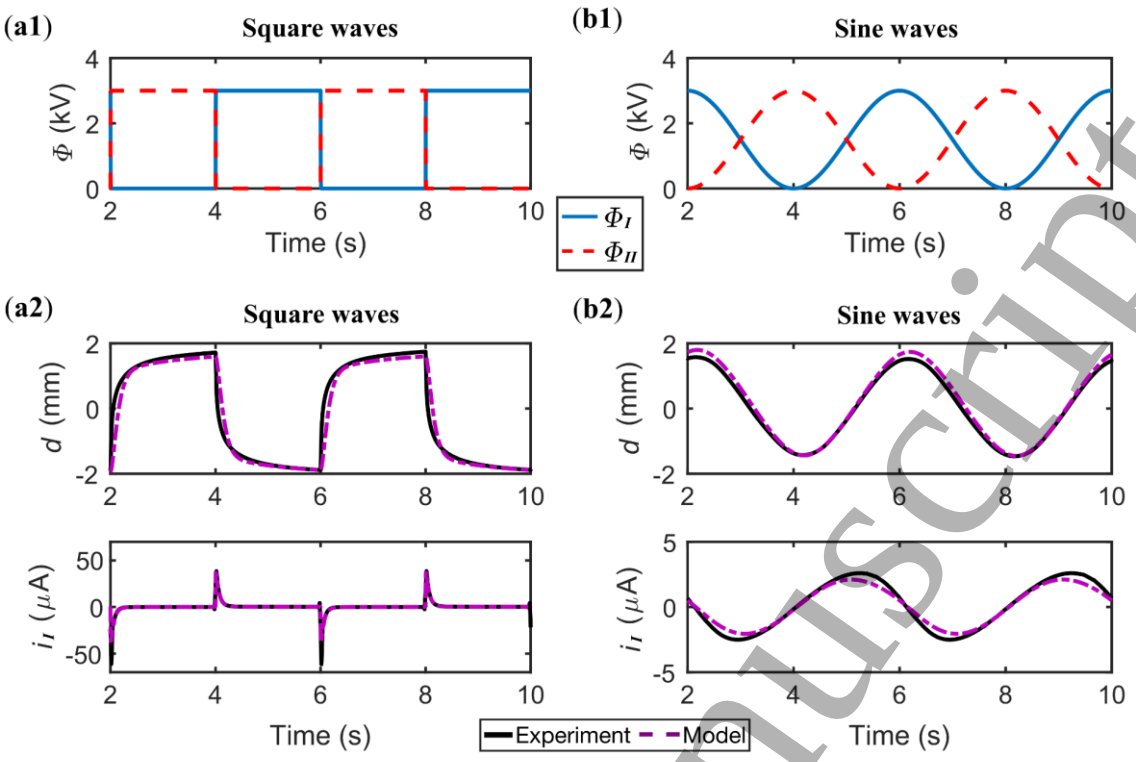

Figure 8. Time series of the displacement and current flow of the DCDEA. (**a1**) Square waves actuation signals and (**a2**) the measured and simulated displacement and current flow. (**b1**) Sinusoidal wave actuation signals and (**b2**) the measured and simulated displacement and current flow. No payload is included in this set of studies.

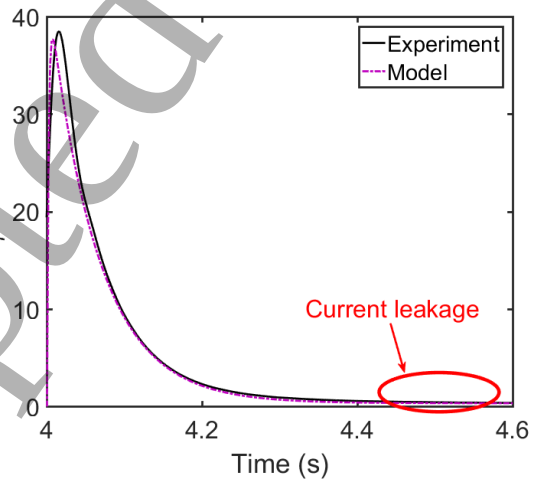

Figure 9. Charging current of the DEA showing a clear current leakage after the DEA reaches a steady charged state.

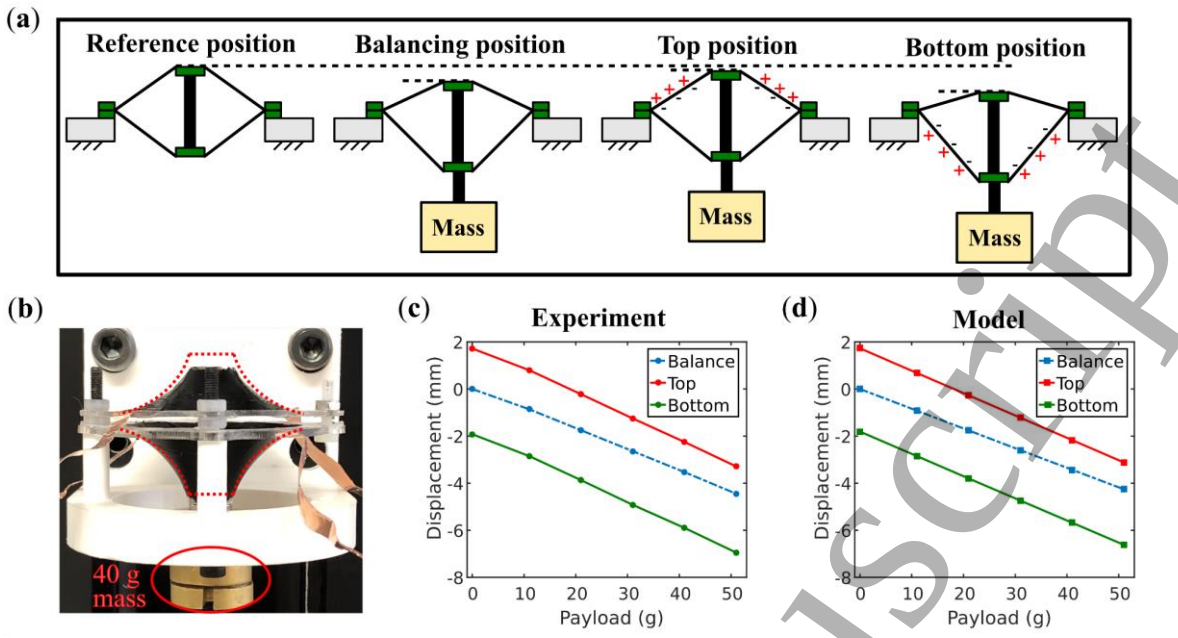

Figure 10. Performance of the DCDEA against payload. (**a**) Schematic diagrams of DCDEA actuation against a payload attached. (**b**) Photo of a DCDEA with 40 g mass attached, the red dash curves indicate the reference position of the DCDEA without payload. (**c**-**d**) Experimental and modelled positions (top, balancing, and bottom) of the DCDEA with varying weights attached. Square actuation waves with the amplitude of 3 kV and frequency of 0.25 Hz are used.

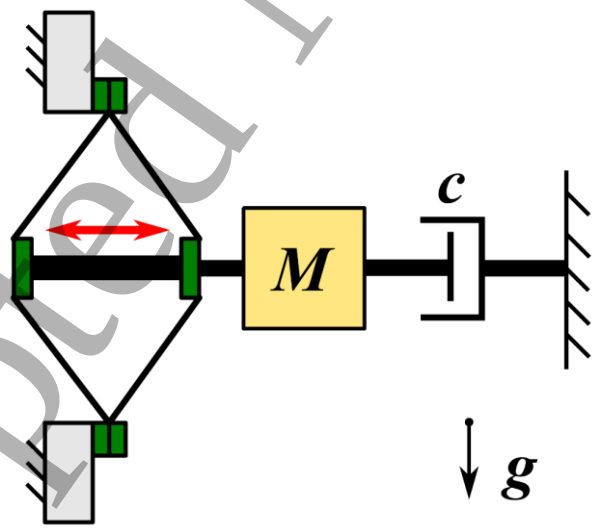

Figure 11. DCDEA energetic study setup.

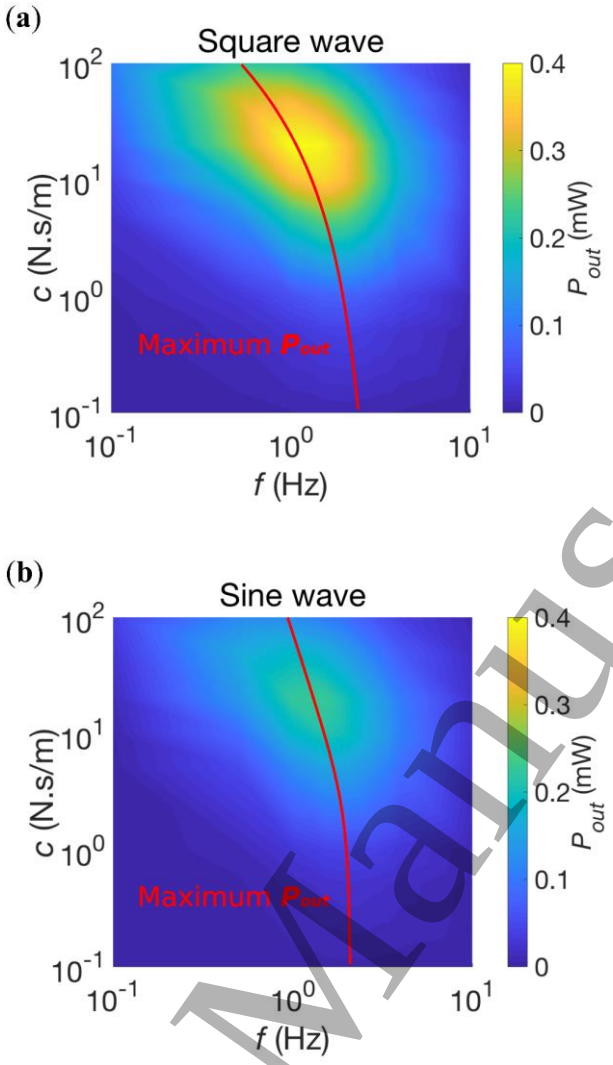

Figure 12. Power output of the DCDEA as a function of frequency and damping coefficient with (**a**) square actuation waves and (**b**) sinusoidal actuation waves.

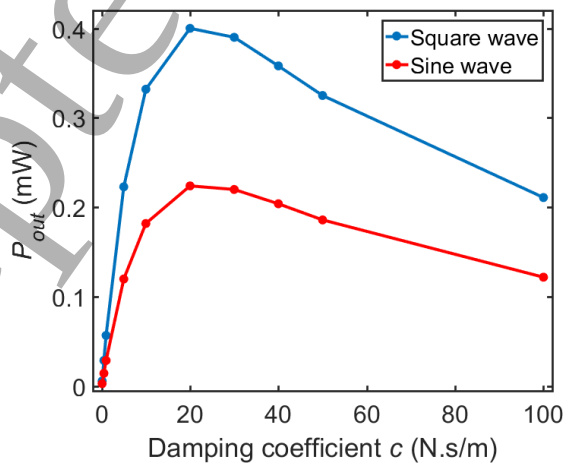

Figure 13. Comparison of the power output of the DCDEA with varying damping coefficients. f = 1 Hz.

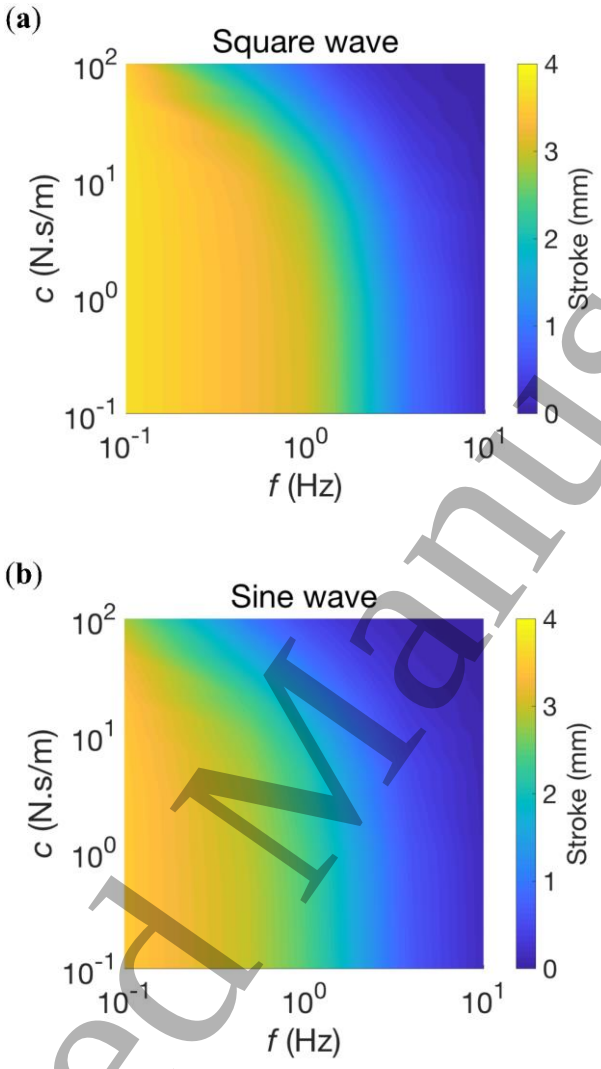

Figure 14. Stroke output of the DCDEA as a function of frequency and damping coefficient with (**a**) square actuation waves and (**b**) sinusoidal actuation waves.

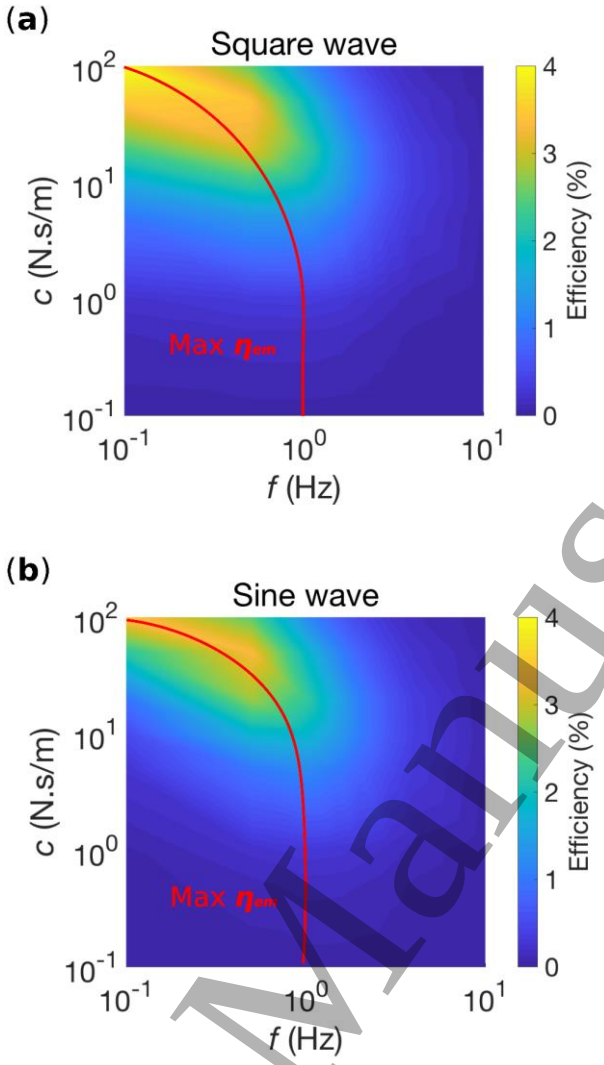

Figure 15. Electromechanical efficiency of the DCDEA as a function of frequency and damping coefficient with (**a**) square actuation waves and (**b**) sinusoidal actuation waves.

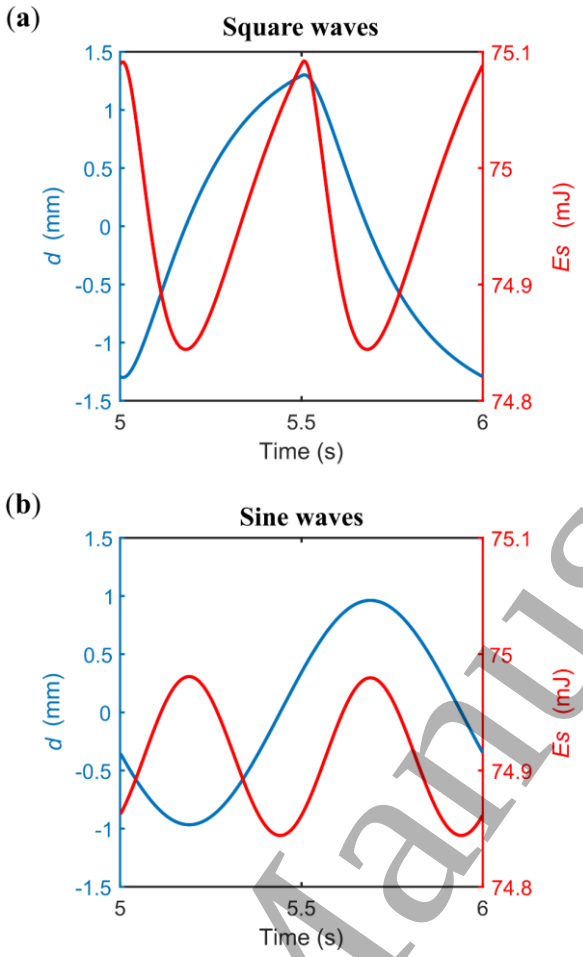

Figure 16. Time series of the displacement and strain energy in one cycle with (**a**) square wave and (**b**) sinusoidal wave. f = 1 Hz, c = 10 N.s/m.

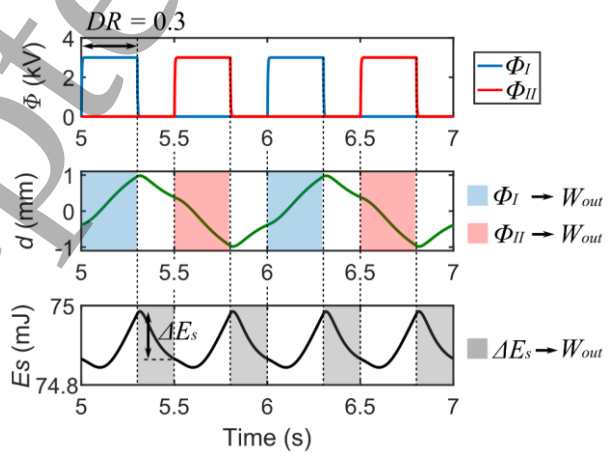

Figure 17. Reducing the duty ratio of the two actuation signals can result in more elastic strain energy stored in the DEA membranes to contribute to the work output.

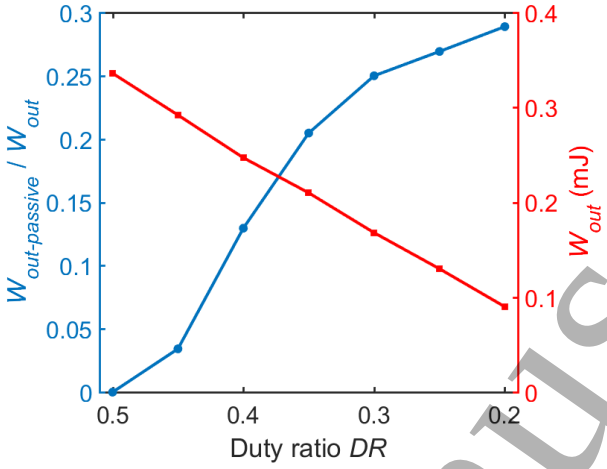

Figure 18. Contribution of the elastic strain energy on the work output and the total work output in one cycle as a function of duty ratio. f = 1 Hz, c = 10 N.s/m.

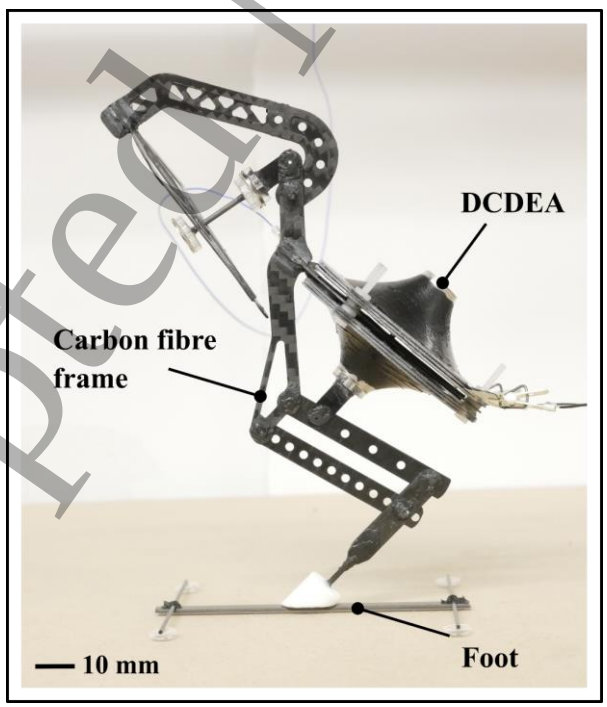

Figure 19. DCDEA driven bio-inspired robotic leg design.

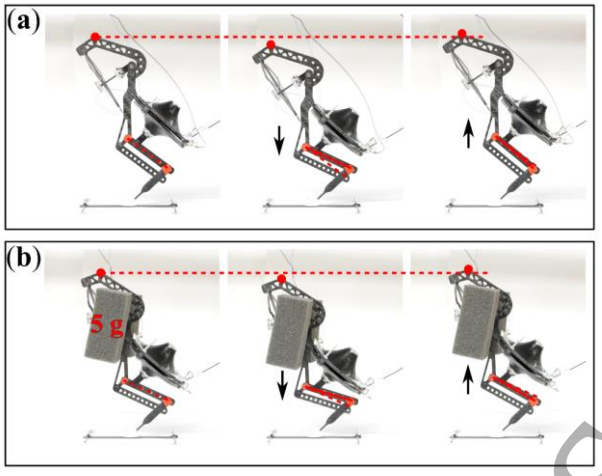

Figure 20. Robotic leg demonstrating a squat motion with (**a**) no additional payload attached and (**b**) 5 g mass attached. (f = 1 Hz in both cases).

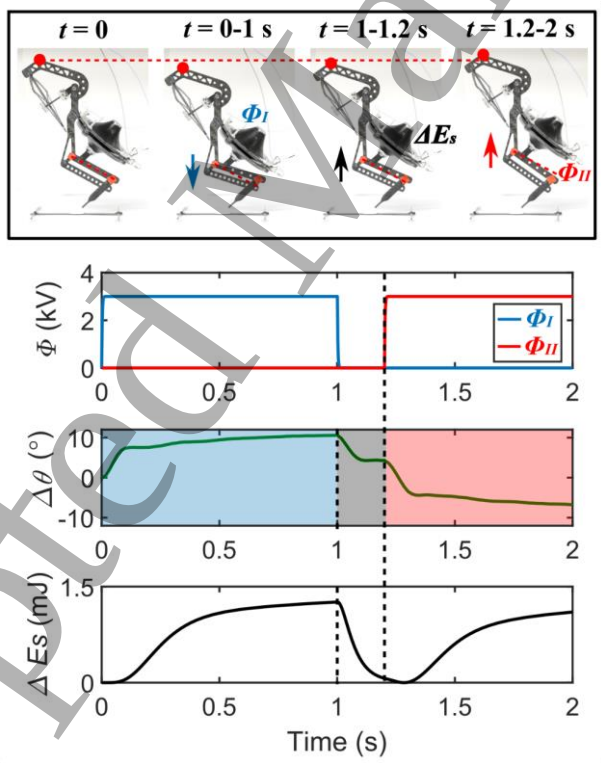

Figure 21. Demonstration of elastic energy recovery with the bio-inspired robotic leg. The input voltages to each membrane, Φ_I and Φ_{II}, the knee angle, θ, and the sum of changes to the elastic strain energy across both membranes from the passive state, ΔE_s, are plotted against time.